



State-of-the-art of Radar Remote Sensing: Fundamentals, Sensors, Image Processing, and Applications

Estado da Arte do Sensoriamento Remoto por Radar: Fundamentos, Sensores, Processamento de Imagens e Aplicações

Edson Eyji Sano ¹, Eraldo Aparecido Trondoli Matricardi ² and Flávio Fortes Camargo ³

¹ Embrapa Cerrados, Planaltina, Brasil. edson.sano@embrapa.br

ORCID: <https://orcid.org/0000-0001-5760-556X>

² Universidade de Brasília, Departamento de Engenharia Florestal, Brasília, Brasil. E-mail. ematricardi@unb.br

ORCID: <https://orcid.org/0000-0002-5323-6100>

³ Departamento Nacional de Infraestrutura de Transportes, Brasília, Brasil. E-mail. flavio.camargo@dnit.gov.br

ORCID: <https://orcid.org/0000-0002-7815-7919>

Recebido: 08.2020 | Aceito: 11.2020

Abstract: This article discusses the state-of-the-art of radar remote sensing and was prepared as part of the special edition of the 50th anniversary of this journal. This study briefly introduces the fundamentals of radar remote sensing, highlighting the most important aspects of image acquisition modes and biophysical parameters of the Earth's surface involved in the process of acquiring radar images. We emphasized wavelength, polarization of electromagnetic waves, image acquisition geometry (imaging parameters), soil and vegetation water content, terrain roughness, and vegetation structure (biophysical parameters of the Earth's surface). Subsequently, the main orbital synthetic aperture radar sensors currently in operation and the main options of radar image processing are presented, highlighting the conversion of digital values to backscatter coefficients, spatial filters to reduce speckle noise, image decomposition techniques, and InSAR processing. Finally, we briefly discuss some potential applications, with special attention to the monitoring of oil spills in continental platforms, above-ground biomass estimation, deforestation monitoring in tropical forests, detection of irrigated rice cropping areas, and soil moisture estimation.

Keywords: SAR. Remote sensing. Backscattering. Earth Resources Satellites.

Resumo: Este artigo aborda o estado da arte do sensoriamento remoto por radar e foi elaborado para fazer parte da edição especial de comemoração dos 50 anos desta revista. Neste estudo, é apresentada uma breve introdução sobre os fundamentos do sensoriamento remoto por radar, com destaque para os parâmetros mais importantes de imageamento e da superfície terrestre envolvidos no processo de obtenção de imagens de radar. Ênfase é dada para o comprimento de onda, polarização das ondas eletromagnéticas e geometria de obtenção de imagens (parâmetros de imageamento) e para a umidade de solos e da vegetação, rugosidade do terreno e estrutura da vegetação (parâmetros da superfície terrestre). Em seguida, são apresentados os principais sensores orbitais de radar de abertura sintética que estão atualmente em operação e os principais processamentos digitais de imagens de radar, destacando-se a conversão dos valores digitais para coeficientes de retroespalhamento, os filtros espaciais para redução do ruído *speckle*, as técnicas de decomposição de imagens e o processamento InSAR. Finalmente, é apresentada uma breve discussão sobre algumas aplicações potenciais, com especial atenção para o monitoramento de derrame de óleo em plataformas continentais, estimativa de biomassa aérea, monitoramento de desmatamento em coberturas florestais tropicais, detecção de áreas de plantio de arroz irrigado e estimativa de umidade de solos.

Palavras-chave: SAR. Sensoriamento remoto. Retroespalhamento. Satélites de recursos terrestres.

1 INTRODUCTION

Radar remote sensing was first used in Brazil by the RADAMBRASIL project during the 1970's for mapping natural resources of Brazil. This project was initially planned to cover the Brazilian Amazon, but it was extended to the entire country in 1975. It consisted of obtaining radar images in analogic format by the U.S. Caravelle airplane carrying a side-looking airborne radar system named GEMS (Goodyear Mapping System 1000), which operated at wavelength of 3.2 cm (X-band), HH polarization, swath of 37 km, north-south flight direction, and lateral overlapping of 25% (LIMA, 2014). These images were made available in hardcopy at 1:250,000 scale and regular grid of 1° 00' x 1° 30'. The rationale of using a radar system was based on its capacity to obtain images regardless of cloud cover and solar illumination conditions. Experts were hired by the Ministry of Mining and Energy to visually interpret the semi-controlled, A0 paper size mosaics to produce soil, geomorphology, geology, and vegetation maps, among other thematic maps. The reports are freely available for download in the library of the Brazilian Institute for Geography and Statistics (IBGE) (<https://biblioteca.ibge.gov.br/index.php/>).

The first spaceborne synthetic aperture radar (SAR) system was launched in 1978 onboard the SEASAT satellite operated by the National Aeronautics and Space Administration (NASA). It was primary designed for global satellite monitoring of oceanographic phenomena and to assist in determining the requirements for satellite remote sensing of oceans (EVANS et al., 2005). Specific objectives included gathering data of sea surface winds and temperatures, wave heights, atmospheric water, and sea-ice properties, among other phenomena in the Earth's surface. In 1981, 1984, and 1994, the Shuttle Imaging Radar (SIR) series was launched and called SIR-A, SIR-B, and SIR-C/X-SAR (CIMINO; ELACHI; SETTLE, 1986; EVANS, 2006). The scientific legacy of these space shuttle missions is extensive, for example, in the fields of biomass estimation, soil moisture, and monitoring of the Amazon rainforest (e.g., STONE; WOODWELL, 1988; HESS et al., 1995; FERRAZOLI et al., 1997; SAATCHI; SOARES; ALVES, 1997; ALSDORF; SMITH; MELACK, 2001). Thanks to the success of space shuttle missions, in the early 1990's, three SAR satellite systems were launched by the European Space Agency (ESA), Canadian Space Agency (CSA), and Japan Aerospace Exploration Agency (JAXA), the Earth Resources Satellite (ERS-1), the RADARSAT-1, and the Japanese Earth Resources Satellite-1 (JERS-1), respectively. These satellites operated at single frequency and single polarization because of the huge volume of data that are generated by SAR systems. Several researchers analyzed the potential of SAR data acquired by these satellites to estimate different biophysical parameters (e.g., DOBSON; PIERCE; ULABY, 1996; SANO et al., 1998a; SRIVASTAVA et al., 2003). However, there was an increasing demand from the scientific community for the capability of multiple polarization, to improve the potential of discriminating/mapping specific targets of interest (e.g., soil moisture) by minimizing the influence of other biophysical parameters (e.g., soil roughness, vegetation structure, and biomass). Capability of dual or full-polarization was only made available in the last generation of radar satellites launched after 2005.

The most recognized advantage of radar sensors is their capability to obtain images regardless of cloud cover conditions (HENDERSON; LEWIS, 1998; SANO; MENESES; ALMEIDA, 2019). This is because wavelengths of spectral bands of SAR sensors are much larger than the average diameter of particles and molecules found in the atmosphere. As a result, SAR systems are more suitable than optical sensors to monitor the environmental dynamics of tropical countries of South America (e.g., Brazil, Guyana, and Peru), Central Africa (Congo, Democratic Republic of the Congo, and Gabon), and Southeast Asia (Indonesia, Malaysia, and Singapore). These regions are well-known for persistent cloud cover conditions throughout the year. Another advantage of SAR data is their independence of solar illumination conditions, which is a disturbing effect in optical remote sensing. We can foresee the following trends in the field of radar remote sensing: increasing availability of no-cost data (so far, there is only one radar satellite data freely available to download on the internet); increasing availability of cloud and storage computing platforms similar to Google™ and Amazon™ to access and process radar images; continuity of existing SAR programs and the release of new programs, ensuring the construction of long and consistent time series of radar data; and availability of ready-to-use SAR products, reducing labor, time, and complex processing commonly observed in radar data analyses.

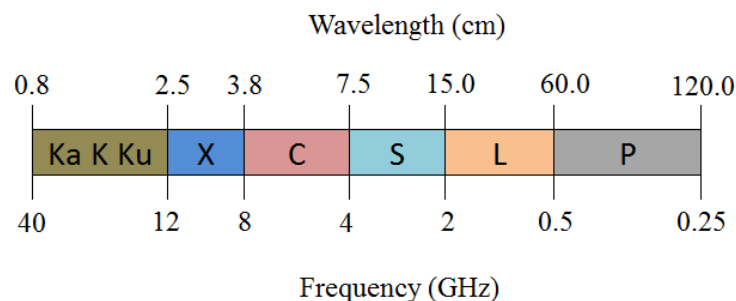
This paper review presents the state-of-the-art of radar remote sensing. It was prepared to be part of

the special edition of the 50th anniversary of this scientific journal. In Section 2, we discuss the fundamentals of radar remote sensing. In Sections 3 and 4, we present the current operating SAR systems and the Brazilian R99B SAR sensor, respectively. In Section 5, we selected some examples of applications. Concluding remarks are presented in Section 6.

2 FUNDAMENTALS OF RADAR REMOTE SENSING

SAR is an active system that operates in the microwave spectral region (approximately from 0.8 cm to 120 cm) (Figure 1). Active systems use their own source of electromagnetic radiation, usually an antenna that transmits pulses of energy and registers the backscattered component of emitted radiation. Backscattering is a term used for active sensors and is equivalent to the reflected solar energy detected by passive sensors. The spectral bands of SAR systems are specified by the following codes: K (0.8 cm – 2.5 cm); X (2.5 cm – 3.8 cm); C (3.8 cm – 7.5 cm); S (7.5 cm – 15 cm); L (15 cm – 60 cm); and P (60 cm – 120 cm). There is no practical meaning for each code described by these capital letters. Developers used ordinary alphabetic descriptors for real wavelengths or frequencies during World War II (JENSEN, 2000). The corresponding intervals of frequency can be used to specify spectral bands as well. Usually, engineers prefer frequencies because when radiation crosses materials with different densities, the frequency is constant, while application researchers prefer wavelengths. In this study, the wavelength was chosen to designate the spectral band of different sensors. Currently, only the X-, C-, and L-bands are used in satellite platforms and there is no satellite system operating with two or three different bands. The longer the wavelength, the stronger the penetration capability of signals emitted on vegetation canopies or soil surfaces. In dry soils, the penetration capability of radar signals is half of its wavelength at the maximum. On vegetation canopies, it will depend on biomass level and vegetation structure. Therefore, the selection of the best wavelength will depend on the type of application or purpose of the study.

Figure 1 – Band designation according to the wavelength and frequency of SAR systems used for gathering information from either airborne or satellite platforms.



Source: Modified from Ouchi (2013).

Another important imaging parameter of SAR systems is the polarization of emitted and backscattered energies. As active sensors, SAR systems can setup the antenna to transmit and receive electric components of signals in a single plane perpendicular to the direction of propagation. Commonly, radar systems are designed to operate in horizontal (H) and vertical (V) planes. As a transmitted signal depolarizes when reaching the terrain, a specific sensor can operate in four different polarization combinations, HH, HV, VH, and VV. The first letter refers to the transmitted signal while the second letter refers to the backscattered signal. HH and VV signals are known as co-polarized signals, while HV and VH signals are known as cross-polarized signals. Usually, co-polarized signals are stronger than cross-polarized signals. Radar systems can have one, two or all four combinations of transmit/receive polarization. Whenever a SAR sensor operates with full polarization capability, there is opportunity to generate RGB color composites of HH, HV or VH, and VV polarized images. When the system operates with two polarizations, we can generate a third image by applying any mathematical operation, such as addition, subtraction, division, multiplication or averaging.

When an antenna emits a pulse of energy towards the terrain, we need to consider the following directions and angles: azimuth and range directions; and incidence or depression angle. Azimuth direction

refers to the direction of the movement of a platform (aircraft or satellite) in a straight line. Pulses of energy in the microwave spectral region are transmitted to the terrain perpendicular to the azimuth direction, which is named range direction. Features in the terrain (e.g., geological structures, such as faults) located perpendicular to the range direction usually are much enhanced in relation to the same features located parallel to the range direction. Depression angle (γ) is the angle formed between the horizontal plane and the pulse of energy emitted by the antenna towards the terrain, while incidence angle (θ) is the angle formed between the line perpendicular to the terrain and the pulse of energy emitted by the antenna. When the terrain is plane, depression angle and incidence angle are complementary.

According to the particle model of the electromagnetic radiation ($E = hc/\lambda$, where E = energy; h = Planck constant; and λ = wavelength), the energy in the microwave spectral region is insufficient to interact with the atoms and molecules of materials to extract information about their chemical composition, which is the basis of optical remote sensing. Thus, extracting information from radar images is based on geometric and dielectric properties of materials (PARADELLA et al., 2005). In other words, soil moisture, terrain roughness, vegetation water content, and vegetation structure play the major roles in radar image analysis. When a dry soil is moisturized, we can visually see when it becomes darker due to increasing absorption of electromagnetic radiation in the visible interval of the electromagnetic spectrum. The same soil becomes brighter in SAR images because there is an increase in the soil dielectric constant (ϵ). Dry soils have low dielectric constant ($3 < \epsilon < 8$), while ϵ of liquid water is around 48-80, depending on its temperature (SANO; MENESES; ALMEIDA, 2019). Therefore, when soil water content increases, ϵ increases and, consequently, the backscattered energy is more intense. The same interaction occurs when there is an increase in the water content of leaves that are photosynthetically active. These soil and vegetation changes and effects are important for being the rationale for using radar data to estimate soil moisture content or phytophysionomies.

Terrain roughness also plays an important role in the backscattering process, since the magnitude of soil roughness is approximately the same magnitude of microwave wavelengths (centimeters). Terrain roughness can be smooth or rough. Smooth surfaces cause near specular reflection of emitted energy, appearing dark in SAR images, while rough surfaces backscatter the emitted energy more intensively, appearing bright in SAR images. The concept of terrain roughness is wavelength- and incidence angle-dependent, that is, a surface can be rough for shorter wavelengths or larger incidence angles, but smooth for longer wavelengths or smaller incidence angles. Although estimating terrain roughness calls little attention in the literature, it is still important to consider its effects, for example, in studies involving estimation of soil moisture and above-ground biomass (AGB). In one of the early studies conducted by Ulaby and Batlivala (1976) using a scatterometer in the field, the authors showed that the influence of soil roughness is less pronounced at the incidence angle of 10° . Quantitative and representative measurements of ground surface roughness in the field to validate estimations derived from SAR images are quite difficult. The time-demanding measurements are acquired by terrain roughness meters or chains. Several measurements are required for a representative measurement of surface roughness of a specific area under study, especially if the area is large or heterogeneous in terms of roughness (NURTYAWAN et al., 2020).

Vegetation structure also strongly affects the backscattering process. Vegetation structure is defined as the proportion of grasses, shrubs, and trees present in an area of interest. Branches and trunks of shrubs and trees act as individual scatterers of emitted radar signals. Therefore, areas with higher density of shrubs and trees will appear brighter in radar images compared with other grass-dominated areas. Thus, radar images can be used to estimate AGB or monitor deforestation (see Section 6 for more details). Some studies have demonstrated that radar data is more appropriate than optical data to discriminate representative phytophysionomies of Cerrado (SANO; FERREIRA; HUETE, 2005) and to map dry forests with strong climatic seasonality worldwide (KOYAMA et al., 2019).

More detailed aspects of principles of radar remote sensing such as the viewing geometry, azimuth and range resolutions, topographic displacements, speckle, and Doppler effects can be found in different textbooks available for purchase (e.g., HENDERSON; LEWIS, 1998; JENSEN, 2000; SANO; MENESES; ALMEIDA, 2019) or for free in the internet (e.g., CCRS, 2020).

3 CURRENT SPACEBORNE SAR SYSTEMS

After the launch of the SEASAT satellite, scientists became aware of the potential of SAR in different applications in the fields of geology, agriculture, forest, hydrology, disaster monitoring, and oceanography, among others. Recently, several spaceborne SARs have been launched and new missions are planned to be launched in the near future. The overall trend is that spatial resolution is improving (1-3 meters), although wide-swath with coarser resolution (~ 100 m) acquisition mode data have been made available for free to allow global studies (OUCHI, 2013). The conventional single polarization mode is becoming dual or even quad-polarized. The main characteristics of current spaceborne SAR platforms are shown in Table 1.

Table 1 – Image acquisition characteristics of main spaceborne SAR systems for Earth observation in operation. As the polarization and resolution (in range) depend on the image acquisition mode, we have provided below the best options available for each satellite. DLR = German Aerospace Center; ISA = Italian Space Agency; CSA = Canadian Space Agency; ESA = European Space Agency; S1A = Sentinel-1A; S1B = Sentinel-1B; JAXA = Japan Aerospace Exploration Agency. CONAE = Argentina's Space Agency. The RADARSAT constellation is in validation and calibration phase. The temporal resolution of Sentinel-1A and Sentinel-1B satellites is 12 days or 6 days if both satellites are combined. JAXA uses a basic observation plan (BOS) as image acquisition strategy (JAXA, 2017).

Satellite	Agency (Country)	Launch	Band	Polarization	Resolution (m)	Temporal Resolution (days)	Citation
TerraSAR-X	DLR (Germany)	2007	X	Dual-pol	1	11	Pitz and Miller (2010)
TanDEM-X	DLR (Germany)	2010	X	Dual-pol	1	11	Krieger et al. (2007, 2013)
COSMO SkyMed	ISA (Italy)	2007	X	Dual-pol	1	16	Covello et al. (2010)
RADARSAT-2	CSA (Canada)	2007	C	Quad-pol	3	24	Fox, Luscombe and Thompson (2004)
RADARSAT Constellation Mission	CSA (Canada)	2019	C	Quad-pol	1	4	CSA (2020)
Sentinel-1A and Sentinel-1B	ESA	2014 (S1A) 2016 (S1B)	C	Dual-pol	5	12 (6)	Torres et al. (2012)
ALOS-2	JAXA (Japan)	2014	L	Quad-pol	3	BOS	Rosenqvist et al. (2014)
SAOCOM	CONAE (Argentina)	2018	L	Quad-pol	10	16	ESA (2020)

Source: The authors (2020).

The number of countries that launched satellites carrying SAR sensors is relatively small. Canada, Japan, and ESA, an intergovernmental organization with headquarters in Paris, France, have vast experience on radar remote sensing, since they launched the first SAR satellites in 1990's, operating with C-band (Canada and ESA) and L-band (Japan). The maintenance of experiences obtained at specific bands by each country is a clear tendency. Germany and Italy have invested in X-band. More recently, Argentina joined the SAR community equipped with L-band through the SAOCOM satellite, launched in 2018.

The constellation of two C-band, 5-meter spatial resolution, 12-day repeat cycle satellites, Sentinel-1A and Sentinel-1B, launched on April 2014 (Sentinel-1A) and April 2016 (Sentinel-2B) in the same orbital plane, is unique because it is the only updated and full SAR data that is freely available on the internet. Images can be downloaded from the ESA's Copernicus Open Access Hub platform, after self-registration, or in cloud processing environments such as the Google Earth Engine™ platform. A number of papers have been already

published using Sentinel-1A and Sentinel-1B datasets in several applications, including monitoring of wildfire (BAN et al., 2020), crop plantations (LA ROSA et al., 2019; MANDAL et al., 2020; SCHLUND; ERASMI, 2020), flooding events (ZHANG et al., 2020), and tropical rainforests (PULELLA et al., 2020). This indicates that an open access policy is one of the best ways to improve and enhance the use and application of radar data. The combination of both Sentinel-1A and Sentinel-1B datasets has the advantage of improving the temporal resolution to 6 days.

The TanDEM-X mission from the German Aerospace Center (DLR) is also unique because of the twin TerraSAR-X and TanDEM-X satellites orbiting in bistatic mode (SAR instruments of both spacecraft look simultaneously at a common footprint from close but with distinct orbital plane), which were launched with the primary objective of generating a global, consistent, and high-resolution digital elevation model (DEM) with unprecedented accuracy (KRIEGER et al., 2007; RIZZOLI et al., 2017). Recently, the TanDEM-X interferometric dataset was used to produce a global forest/non-forest map (MARTONE et al., 2018). The next generation of the spaceborne SAR missions will adopt the concept of SAR tomography to acquire 3-D images from the terrain, after the launch of TanDEM-L by DLR (MOREIRA et al., 2015; NANNINI et al., 2019). This mission concept comprises two fully polarimetric radar satellites with large antenna apertures (array-fed reflector principle) which will enable, for the first time, to image a continuous 350-km swath with a 7-m azimuth resolution (HUBER et al., 2018). Several applications can benefit from SAR tomography, including deforestation monitoring by taking advantage of differences in the three-dimensional forest structure. DLR is the only space agency holding the bistatic technology.

4 THE BRAZILIAN R99B SAR

In the early 2000s, the Brazilian Air Force operated two X- and L-band SAR sensors onboard R99B aircrafts, focused mainly on surveillance of the Brazilian Amazon. The images were made available at the spatial resolutions of 3, 6, and 18 m, with full polarization (HH+HV+VH+VV) for the L-band and single polarization (HH) for the X-band, with swathes of 20 km, 40 km, and 120 km.

Several studies were conducted based on this system. Simulated images of the proposed L-band, German-Brazilian SAR satellite named Multi-Application Purpose SAR (MAPSAR) were obtained by the R99B aircraft (Mura et al., 2009). Alves et al. (2009) developed a methodological approach to identify illegal airplane strips in the municipality of Itaituba, Pará State. Other studies involved deforestation discrimination in the Brazilian Amazon (GUERRA; MURA; FREITAS, 2010), geomorphological mapping in the municipality of Iranduba, Amazonas State (PINTO; LUCHIARI, 2017), gold mining in the Tapajós Mineral Province (CARRINO et al., 2011), iron-mineralized laterites in the Carajás Mineral Province (SILVA et al., 2013), and discrimination of coastal wetland environments (SOUZA-FILHO et al., 2011). Unfortunately, MAPSAR was never launched and R99B SAR is not operational anymore.

5 SAR IMAGE PROCESSING

When SAR raw data are pre-processed, the resulting product is in a complex format referred as single-look complex (SLC), containing data of amplitude and phase. The amplitude of each pixel is proportional to the magnitude of radar backscatter and depends on SAR geometry, wavelength, polarization, and geometric and dielectric properties of targets (OUCHI, 2013). Considering that there are several scatterers within a SAR resolution cell, each individual scatterer backscatters the emitted signals in different times, which is a characteristic related to the phase information in radar image analysis. Phase represents the point in the wave of the backscattered signal when it reaches the antenna, being measured in radians or degrees. The amplitude is the real part of the complex value, while the phase is the imaginary part. In practical terms, the phase of a single image can be exploited for polarimetric decomposition, generation of interferograms or DEMs. In this section, we present further details on the main processing steps involved with geocoding, target decomposition, and InSAR processing.

5.1 Geocoding

Although users have the option to order SAR images already projected from slant range to ground range and geocoded using some DEM, in this section we will present the most important steps to convert SLC data into backscattering coefficients (σ° , units in decibels) and to geocode images. Geocoding is important to allow SAR data to be integrated with other types of geospatial data (e.g., other satellite images and vector-based maps). The conversion of SLC data into σ° geocoded data involves the following steps:

- a) radiometric calibration;
- b) multilook filtering;
- c) speckle filtering;
- d) conversion of digital number into σ° ; and
- e) geocoding.

All steps previously described can be conducted using open-access software such as the Sentinel Application Platform (SNAP) (ESA, 2019) or using commercial software, such as the L3 Harris Geospatial ENVI SARscape™ (SARMAP, 2020). Radiometric calibration converts digital numbers into radiometrically calibrated backscatter and usually is fully automated by using a software previously mentioned or any other appropriate software, since all information required is included in the metadata file of the SAR products. This step is important especially when the analyst is preparing data for mosaicking two or more images acquired from different incidence angles and different brightness levels. Ultimately, radiometric calibration can correct SAR images, so that pixel values truly represent the radar backscatter of the targets in the terrain (ESA, 2019).

Multilooking is a process involving slant-range to ground-range conversion, producing data with a nominal pixel size and less noise, since the averaging process involved in this procedure smooths images (ENVI, 2020). For example, a hypothetical sensor with a nominal spatial resolution of 6.25 m can be resized into 5-meter pixel size in this procedure. Thus, processed SAR data are often specified in terms of pixel size rather than in terms of its nominal spatial resolution. When SLC images are filtered using a multilook filter, the resulting intensity (squared amplitude) images are called power images.

Speckle is a type of noise inherent to SAR images caused by random constructive and destructive interference of individual scatterers from the terrain, causing a salt-and-pepper aspect in the images. Then, we apply speckle filters to reduce the blurred features of images. Several filters are available in the literature, such as Lee, Frost, and Gamma Map, for example. Choosing the best speckle filter is not a trivial task because there is no corresponding noise-free image available to compare. Thus, filter quality, which is often site-dependent, is usually evaluated visually in terms of presence of blurring effects in homogeneous areas and preservation of surface feature details in heterogeneous areas (ARGENTI; LAPINI; ALAPARONE, 2013).

Digital numbers (DN) are converted into σ° (dB) by the following equation (Eq. 1):

$$\sigma^\circ (dB) = -10 * \log (DN^2) + CF \quad (1)$$

Where CF = calibration factor, which depends on each sensor.

Alternatively, some authors use γ° instead of σ° ; γ° is the σ° corrected by the local incidence angle (θ) (Eq. 2):

$$\gamma^\circ (dB) = \sigma^\circ / \cos (\theta) \quad (2)$$

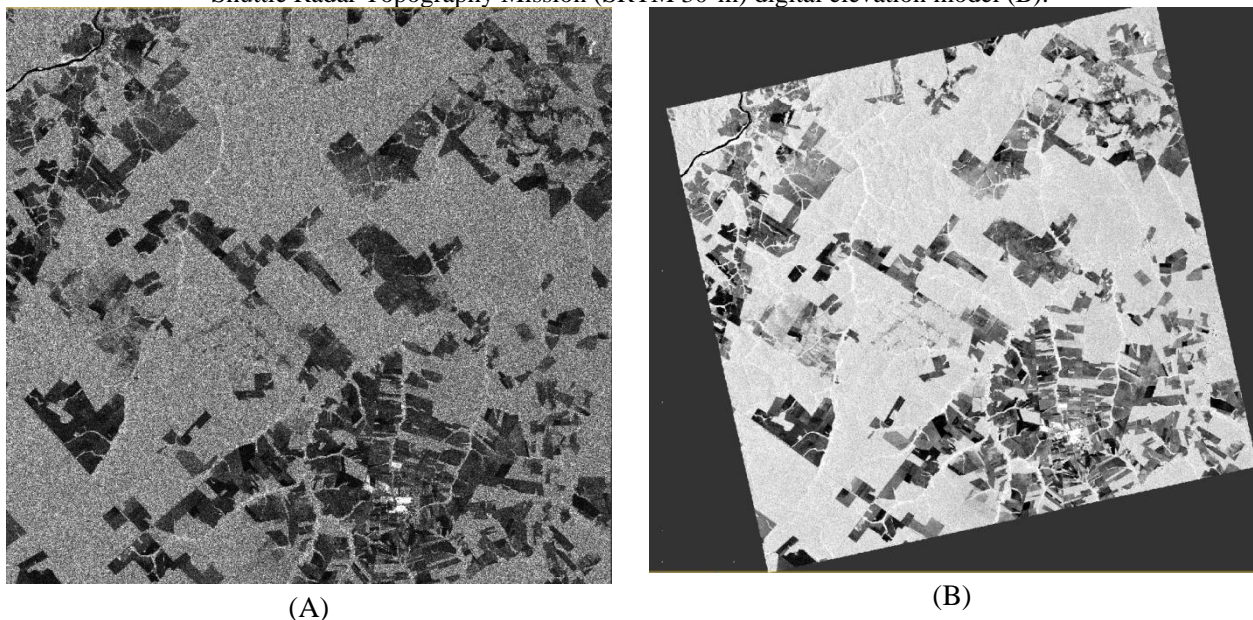
Typically, σ° values range from -32 dB to +16 dB. Co-polarized values are commonly higher than cross-polarized values. The lowest values are usually found in targets causing specular reflection of emitted energy (e.g., clear water bodies without wind). On the other hand, the highest σ° values are found in targets causing double-bounce reflections (e.g., urban areas with buildings distributed perpendicular to the range

direction of the SAR sensor).

The geocoding procedure requires the use of a DEM for terrain correction and to insert a coordinate system in the final SAR product. Although the previously mentioned software has its own models, users can choose other elevation models. The most common DEMs freely available on the internet include the Shuttle Radar Topography Mission (SRTM-3 Version 4, 30-m resolution) and the ASTER Global DEM (GDEM). NASA has released a new NASA DEM product (30-meter resolution) without many limitations and restrictions in relation to the popular SRTM DEM product and with increased accuracy and covered area. JAXA also released the new version of the ALOS World 3D-30m (AW3D30) dataset, produced based on the PRISM panchromatic optical sensor onboard the ALOS-1 satellite that operated from 2006 to 2011 (TAKAKU; TADONO; TSUTSUI, 2014). DLR has produced a global DEM with unprecedented accuracy (12-m horizontal resolution and 2-m relative height accuracy) using TerraSAR-X and TanDEM-X satellites flying in close formation (ZINK et al., 2014). This product, however, is not freely available to download on the internet.

Figure 2 illustrates an example of HH-polarized radar image from an ecotone region located between Amazonia and Cerrado biomes (municipality of Sinop, Mato Grosso State, and surroundings) acquired by ALOS-2 satellite in February, 2016, under the JAXA's Kyoto & Carbon Initiative (ROSENQVIST et al., 2010). The image was acquired in the Stripmap mode, spatial resolution of 6.25 m, and CEOS format. Figure 2A shows the image acquired in slant range geometry. There are geometric distortions reducing the usefulness of this image, often preventing information extraction. Figure 2B shows the same image processed by radiometric calibration, multilook filtering, Gamma Map speckle filtering, and geocoding using the 30-m SRTM DEM. The image was projected into Universal Transverse Mercator (UTM) projection (UTM fuse = 21S; datum = WGS84). It is observed that SLC images are north-south oriented while geocoded images are ascending or descending oriented. More details of the pre-processing of this image can be found in Silva et al. (2020).

Figure 2 – Illustration of an ALOS-2/PALSAR-2 satellite image acquired in February 12, 2016 in single look complex format (A) and processed by radiometric calibration and multilook and speckle filtering, and geocoded by using the Shuttle Radar Topography Mission (SRTM 30-m) digital elevation model (B).



Source: The authors (2020).

5.2 Polarimetry and target decomposition

Polarimetric SAR data show a large amount of information from terrestrial targets when compared to conventional amplitude, single or dual polarized SAR data (VAN DER SANDEN, 1997; OUCHI, 2013). This is because SAR polarimetry has the ability to describe and store data on changes in the polarization state of the electric field vector (\vec{E}) altered by the structure and ϵ of objects on the Earth's surface (LEE; POTTIER,

2009). The equation of an ellipse is the most common way of representing \vec{E} (HELLMANN; 2001; LEE; POTTIER, 2009; RICHARDS, 2009). The scattering matrix (S) (Eq. 3), or Jones matrix, is used to describe the linear transformation of changes occurring between the electrical vector transmitted by the SAR antenna and the electrical vector scattered by targets. This matrix allows describing target and the acting physical processes (HELLMANN, 2001).

$$[S] = \begin{bmatrix} S_{hh} & S_{hv} \\ S_{vh} & S_{vv} \end{bmatrix} \rightarrow \vec{k} = \frac{1}{2} \text{Trace}([S]\Psi) = [k_0, k_1, k_2, k_3]^T \tag{3}$$

Where [S] is the scattering matrix S; S_{ij} is the complex element of [S]; k_i is the complex element of Jones vector (\vec{k}); Trace [S] is the sum of elements in diagonal of [S]; and Ψ is the matrix base 2x2.

Pauli basis is used to estimate Ψ (Eq. 4) (HELLMANN, 2001; LEE; POTTIER, 2009):

$$\Psi_P = \left\{ \sqrt{2} \begin{bmatrix} 1 & 0 \\ 0 & 1 \end{bmatrix}, \sqrt{2} \begin{bmatrix} 0 & 1 \\ 0 & -1 \end{bmatrix}, \sqrt{2} \begin{bmatrix} 0 & 1 \\ 1 & 0 \end{bmatrix} \right\} \tag{4}$$

Alternatively, Borgeaud basis can be used to estimate Ψ (Eq. 5):

$$\Psi_B = \left\{ 2 \begin{bmatrix} 1 & 0 \\ 0 & 0 \end{bmatrix}, 2\sqrt{2} \begin{bmatrix} 0 & 1 \\ 0 & 0 \end{bmatrix}, 2 \begin{bmatrix} 0 & 0 \\ 1 & 0 \end{bmatrix} \right\} \tag{5}$$

Lee and Pottier (2009) introduced the concept of distributed targets, that is, in SAR imaging, not all targets are stationary or fixed and may vary over time. Natural targets, for example, change due to the wind, temperature, and pressure dynamics. Therefore, the backscattered wave must be considered partially polarized, which means that the wave is no longer coherent, monochromatic, and fully polarized in the form described by the polarization ellipse. Thus, the scattering matrix S has limitations to represent those incoherent targets, which will require covariance and coherence matrices (also called power matrices) to understand areas with predominance of distributed targets. The polarimetric covariance matrix is formed by a crossing product between the Borgeaud vector and its transposed conjugate complex (Eq. 6) (HELLMANN, 2001):

$$[C]_{4 \times 4} = \langle \vec{k}_B \vec{k}_B^{*T} \rangle = \begin{bmatrix} \langle |S_{hh}|^2 \rangle & \langle S_{hh} S_{hv}^* \rangle & \langle S_{hh} S_{vh}^* \rangle & \langle S_{hh} S_{vv}^* \rangle \\ \langle S_{hv} S_{hh}^* \rangle & \langle |S_{hv}|^2 \rangle & \langle S_{hv} S_{vh}^* \rangle & \langle S_{hv} S_{vv}^* \rangle \\ \langle S_{vh} S_{hh}^* \rangle & \langle S_{vh} S_{hv}^* \rangle & \langle |S_{vh}|^2 \rangle & \langle S_{vh} S_{vv}^* \rangle \\ \langle S_{vv} S_{hh}^* \rangle & \langle S_{vv} S_{hv}^* \rangle & \langle S_{vv} S_{vh}^* \rangle & \langle |S_{vv}|^2 \rangle \end{bmatrix} \tag{6}$$

Where $[C]_{4 \times 4}$ is the matrix 4x4 of covariance (diagonal elements represent the signal strength at the respective polarization); $\langle \dots \rangle$ is the spatial average; k_B is the Borgeaud vector; and \vec{k}_B^{*T} is the conjugated complex of the Borgeaud vector.

Another concept of dealing with the non-deterministic or incoherent nature of the backscattered wave consists of estimating a polarimetric coherence matrix (HELLMANN, 2001). This matrix is formed by the crossing product between the Pauli vector and its conjugate complex (Eq. 7):

$$[T]_{4 \times 4} = \langle \vec{k}_P \vec{k}_P^{*T} \rangle \tag{7}$$

By assuming the reciprocity theorem, we can describe it as $S_{hv} = S_{vh}$. In this case, the Pauli vector can be reduced to three dimensions without losing information (Eq. 8) (HELLMANN, 2001):

$$[T]_{3 \times 3} = \langle \vec{k}_{P_3} \vec{k}_{P_3}^{*T} \rangle = \frac{1}{2} \begin{bmatrix} \langle |A|^2 \rangle & AB^* & AC^* \\ \langle A^*B \rangle & \langle |B|^2 \rangle & BC^* \\ \langle A^*C \rangle & \langle B^*C \rangle & \langle |C|^2 \rangle \end{bmatrix} \tag{8}$$

where $[T]_{3 \times 3}$ is the 3x3 coherence matrix; k_p is the Pauli vector; \vec{k}_p^{*T} is the transposed conjugated complex of the Pauli vector; $A = S_{hh} + S_{vv}$; $B = S_{hh} - S_{vv}$; and $C = 2S_{hv}$.

Decomposition techniques aim to represent the average scattering mechanism as a sum of independent elements, associating a physical scattering mechanism to each of those elements. Target decomposition theorems can be classified into two major groups, coherent and incoherent decomposition types. Coherent decompositions assume the occurrence of deterministic scatterers and the backscattered wave is polarized. This target decomposition type uses the scattering matrix S to represent the polarization state of the backscattered wave. On the other hand, incoherent decompositions consider a priori that scattering is not of the deterministic type and the backscattered wave is partially polarized. In this situation, covariance and coherence matrices are used to characterize the backscattered wave (LEE; POTTIER, 2009; RICHARDS, 2009).

In remote sensing applications, the assumption of occurrence of pure deterministic targets is not always valid (RICHARDS, 2009). Thus, power reflection matrices are often used. Based on it, this author described only the incoherent target decomposition methods, with emphasis on the following target decomposition theorems: Yamaguchi (with four components); and entropy (H), anisotropy (A), and α angle (Cloude-Pottier decomposition). The digital image processing of these theorems can be performed, for example, in the SNAP software (ESA, 2018). The images must be in SLC format and in full-polarimetric mode (CAMARGO et al., 2019). In the case of the Cloude-Pottier decomposition, it is possible to generate decompositions of dual-pol SLC images using the SNAP application. Image processing is applied directly to the SLC data without any pre-processing (calibration or filtering), making it optional to use polarimetric filters to remove speckle noise in the matrices. Careful use of polarimetric filters in the matrices is recommended to avoid unnecessary resampling and losing useful information in target decompositions.

Yamaguchi et al. (2005) developed a model for decomposing targets based on covariance matrix modeling consisting of four scattering components, namely: double bounce, surface scattering, volumetric scattering, and helix. The first three components are based on their correspondents presented in the model by Freeman and Durden (1998). The fourth component was introduced by Yamaguchi et al. (2005) and estimates helix-like scattering, which is a target with artificial shape and/or structure, defined as a non-symmetrical reflector capable of generating circular polarizations to the left or to the right, being more suitable for describing artificial targets.

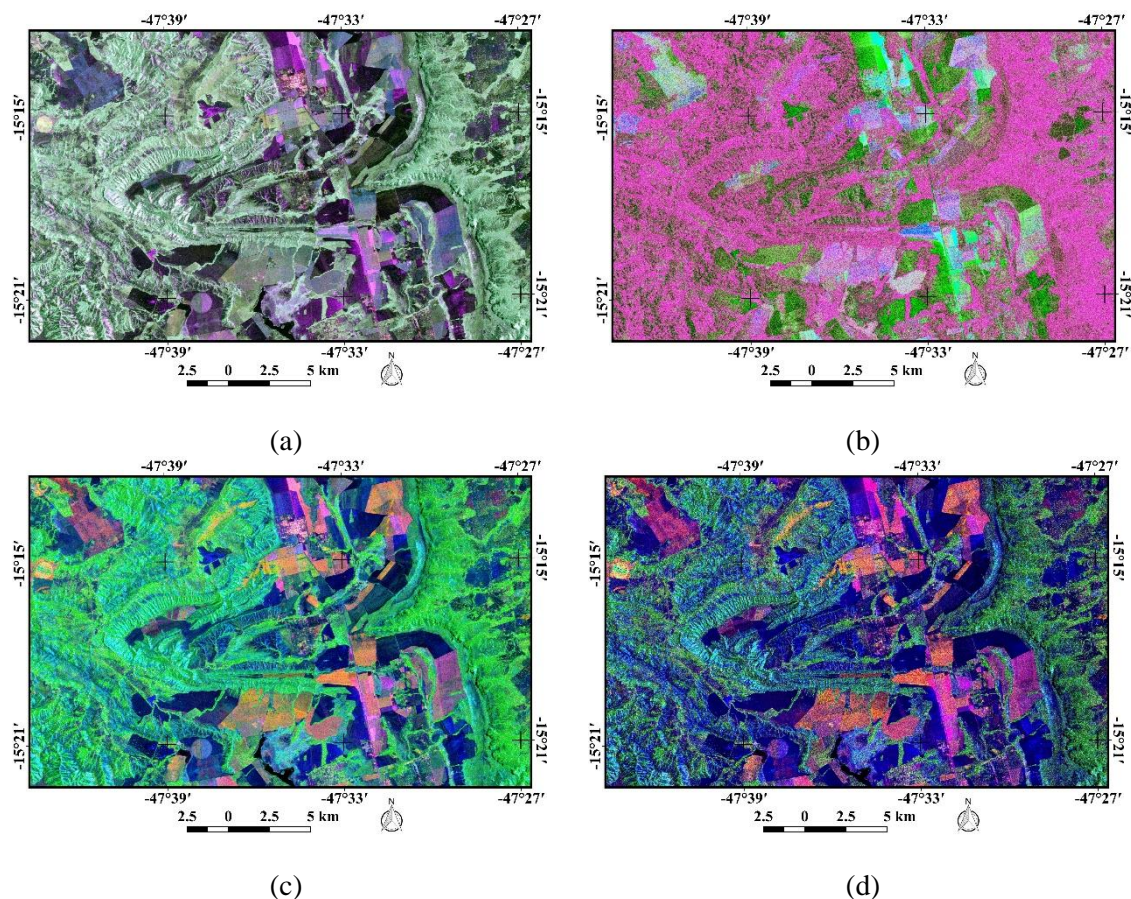
Yamaguchi et al. (2005) also changed the modeling of volumetric scattering to better represent scattering in forested environments. The conventional theoretical model of volumetric scattering consists of a cloud of dipoles of random orientation with modeling based on a function of uniform probability density with different angles of orientation. However, in environments predominantly occupied by vertical structures (such as forest vegetation), scatterings from trunks and branches have preferential distribution angles. These authors adjusted the probability density function by Freeman-Durden considering some aspects of the dominant orientation of tree trunks and branches. Figures 3c and 3d show color composites generated by the components derived from the Yamaguchi theorem.

Cloude-Pottier decomposition can be used to analyze eigenvalues and eigenvectors of the coherence matrix by decomposing that matrix into elements that represent partial scattering, which will include all types of scattering mechanisms, focusing on the analysis of eigenvalues and eigenvectors has the advantage of being basis-independent and always diagonalizable (CLOUDE; POTTIER, 1997; LEE; POTTIER, 2009). In the proposal by Cloude and Pottier, the coherence matrix is decomposed into the sum of three other partial coherence matrices and each individual matrix is weighted by its respective eigenvalue (Eq. 9):

$$[T_3] = \sum_{i=1}^{i=3} T_{3i} = \sum_{i=1}^{i=3} \lambda_i (\vec{e}_i \cdot \vec{e}_i^{*T}) = \lambda_1 (\vec{e}_1 \cdot \vec{e}_1^{*T}) + \lambda_2 (\vec{e}_2 \cdot \vec{e}_2^{*T}) + \lambda_3 (\vec{e}_3 \cdot \vec{e}_3^{*T}) \tag{9}$$

Where $[T_3]$ is the 3x3 coherence matrix; λ_i is the autovalue; and e_i is the autovector.

Figure 3 – RGB colored composites featuring: a) polarized images in amplitude (HH/HV/VV); b) Cloude-Pottier decomposition theorem (H/A/ α); c) Yamaguchi theorem without the Helix component (double/volume/surface); and d) Yamaguchi theorem with the helix component (double/helix/surface). The images correspond to an ALOS-2/PALSAR-2 scene over part of the municipality of Planaltina, Goiás State, acquired on May 16, 2016, ascending orbit, full-polarimetric mode, with pixel spacing of 6.25 m. Horizontal datum: WGS84; projection system: UTM 23S.



Source: The authors (2020).

Each of the individual matrices represents a contribution of a specific type of deterministic scattering. The weight of each contribution is given by the eigenvalue, while the type of scattering mechanism is given by the eigenvector. The main indicators derived from the target decomposition theorem are entropy (H), anisotropy (A), and measurement of α angle (CLOUDE; POTTIER, 1997; LEE; POTTIER, 2009). Figure 3b shows a color composite generated with the components derived from the Cloude-Pottier decomposition theorem. Polarimetric entropy (H) indicates the degree of randomness in the distribution of scattering mechanisms (Eq. 10):

$$H = -\sum_{i=1}^3 P_i \log_3 P_i, \quad P_i = \frac{\lambda_i}{\sum_{k=1}^3 \lambda_k} \tag{10}$$

Values of P_i are interpreted as the relative intensity of i scattering process. Values of H range between 0 and 1; $H = 0$ indicates that the coherence matrix has only one eigenvalue (λ_i) other than 0, representing only a deterministic scattering process. On the other hand, $H = 1$ indicates that the eigenvalues of the coherence matrix are all the same, with a scattering process of random noise type that totally depolarizes the incident wave (CLOUDE; POTTIER, 1997; LEE; POTTIER, 2009). Polarimetric anisotropy is an indicator of the relative importance of secondary scattering mechanisms, which is more representative when medium entropy occurs, given by (Eq. 11):

$$A = \frac{\lambda_2 - \lambda_3}{\lambda_2 + \lambda_3} \quad (11)$$

According to Cloude and Pottier (1997) and Lee and Pottier (2009), in cases of high entropy, anisotropy does not provide any additional information, given that eigenvalues are approximately equal. In cases of low entropy, self-values are close to zero. The average entropy indicates that more than one scattering mechanism is contributing to backscattering, but it does not estimate how many mechanisms. Anisotropy also provides additional information. High anisotropy indicates that only the second scattering mechanism is important, while low anisotropy indicates that there is also contribution of the third scattering mechanism. From the coherence matrix, each eigenvector can also be parameterized in terms of five angles, α , β , φ , δ , and γ , with emphasis on angle α , with variation between 0° and 90° , since it identifies the type of scattering mechanism of the physical target. For α close to 0° , odd bounce isotropic scattering predominates; at 45° , dipole scattering predominates; and at 90° , double bounce scattering predominates (CLOUDE; POTTIER, 1997; LEE; POTTIER, 2009).

5.3 InSAR

SAR interferometry consists of using two or more SLC SAR images from the same geographic area with different acquisition geometries to extract phase differences in each footprint image (HANSSEN, 2002; RICHARDS, 2009). The phase difference obtained between complex images is related to the distance between the two trajectories during each image acquisition, the baseline length (the distance between antennas), the height of the object on the ground, and the wavelength of the SAR system. Thus, the angle of the interferometric phase and, subsequently, the terrain heights are obtained.

Prior to InSAR processing, accurate registration between SLC images needs to be obtained. It is also necessary to filter images in range direction to remove unusual spectral information in the images related to differences in the viewing line of each antenna. This procedure allows noise removal in interferometric phase images. The interferogram is one of the main products of InSAR processing. Due to the cyclic characteristics of the interferometric phase, interferograms present ranges of object height in each 2π cycle (HANSSEN, 2002; RICHARDS, 2009).

After generating the interferogram, phase variations related to changes in incidence angles along the antenna range of the SAR system must be removed. In addition, the interferometric coherence image must be generated to assess the quality of the interferogram in relation to possible errors due to temporal, noise, and spatial decorrelation caused by the antenna baseline. Finally, to generate DEM, the gradient of the phases needs to be integrated over the range distance by adding or subtracting 2π for each discontinuity. To obtain altitudes, control points with known planimetric and altimetric coordinates are used to calibrate the interferogram (HANSSEN, 2002; RICHARDS, 2009).

6 APPLICATION EXAMPLES

Table 2 summarizes some of applications of SAR data, ranging from geology to cryosphere. We did not intend to present a complete list of applications; instead, we provided some comments on potential applications of radar remote sensing for those that are not familiar with this technology.

Table 2 – Potential uses of SAR data in different applications.

Field	Specification
Geology	Structural geology, mineral prospection, DEM generation, landslide monitoring
Forestry	Biomass estimation, deforestation monitoring
Agriculture	Crop yield, crop classification
Hydrology	Soil moisture, flooding
Oceanography	Ship and oil spill detection
Cryosphere	Iceberg movement tracking

Source: The authors (2020).

6.1 Ship and oil spill detection

Ship and oil spill detections are among the top applications of SAR data, especially involving C-band. A substantial amount of papers has been published on these subjects (e.g., LI; HE; WANG, 2009; MIGLIACCIO et al., 2012; DECHESNE et al., 2019). Research on ship detection is mainly related to checking international maritime requirements, identifying illegal operating ships, and surveilling piracy (OUCHI, 2013). For example, most of oil pollution from ships is linked to routine operations, such as tank washing, rather than accidents (ALPERS; HOLT; ZENG, 2017). The major drawback of ship identification by SAR is the relatively low spatial resolution of spaceborne SAR for this type of application.

Pollution of sea surface by petroleum is also a major environmental concern because of accidents such as the one in the Gulf of Mexico in 2010 (LAVROVA; KOSTIANOY, 2011; LEIFER et al., 2012). Thus, it is very important to continuously monitor activities of petroleum platforms. Surface tension of oil is greater than that of water so that oil slicks observed in ocean surfaces drastically reduce the centimeter-scale Bragg waves that are responsible for radar backscattering, causing specular reflection of incident microwave signals. Consequently, oil spills appear as dark patches in the ocean. Lower wavelengths such as X- and C-band are more suitable for this purpose as the damping effect of Bragg waves is higher for shorter wavelengths. VV-polarization is preferred than HH-polarization because of its higher backscattering process in the sea surface (VALENZUELA, 1978). However, developing algorithms to identify oil spills unambiguously on radar images is not an easy task. According to Alpers, Holt and Zeng (2017), there are 13 potential sources of phenomena that can be related to dark patches in the ocean, with plankton and low winds probably being the two most important ones. If the wind speed is lower than 3-4 m s⁻¹, the sea surface can also appear dark, hampering the identification of oil leak (IVANOV, 1998). If dark patches are linked to offshore oil platforms, as shown in Figure 4, the chances that patches are related to planktons or winds reduces.

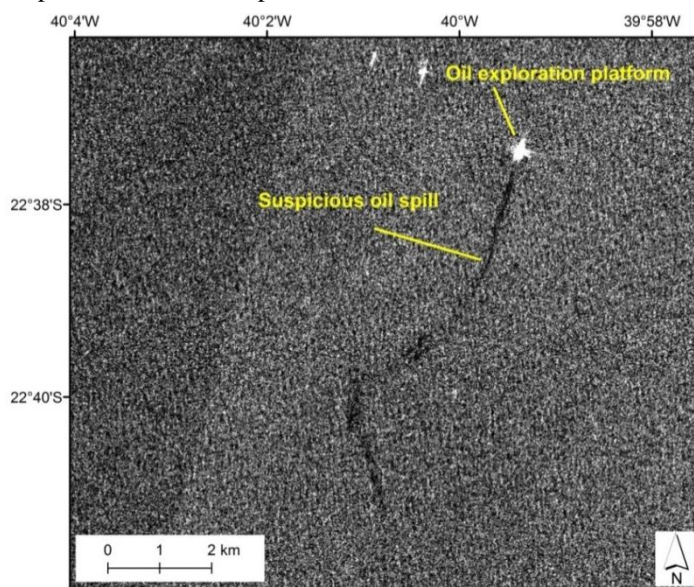
6.2 Forest monitoring

SAR products can also be applied to extract forest information mainly over tropical countries, including estimation of above-ground carbon stocks and monitoring clear-cut deforestation, selective logging, and secondary regrowth. For carbon stock estimation, the general rule is that backscattered signals increase with increasing biomass levels. Longer wavelengths penetrate deeper into the forests, so that L-band usually provides more accurate biomass estimations, since branches and trunks are the major constituents of AGB. The dominant scattering processes at the X- and C-bands occur in the top of canopy layers. It is also known that cross-polarization correlates better than co-polarization with tree biomass. HV polarization is most sensitive and VV, the least sensitive (KASISCHKE; MELACK; DOBSON, 1997).

Because of the relevance of the Brazilian Amazon in terms of biodiversity conservation and climate change mitigation, several studies evaluating the potential of SAR technology to detect and monitor deforestation have been published (e.g., ALMEIDA-FILHO et al., 2005; PEREIRA et al., 2016; HAGENSIEKER; WASKE, 2018). Clear-cut deforested areas appear as dark patches in SAR images due to the decrease of AGB, plant water content, and volume scattering from wood debris on the ground (Figure 5). However, depending upon the time lag between deforestation and SAR overpass, deforested areas can appear

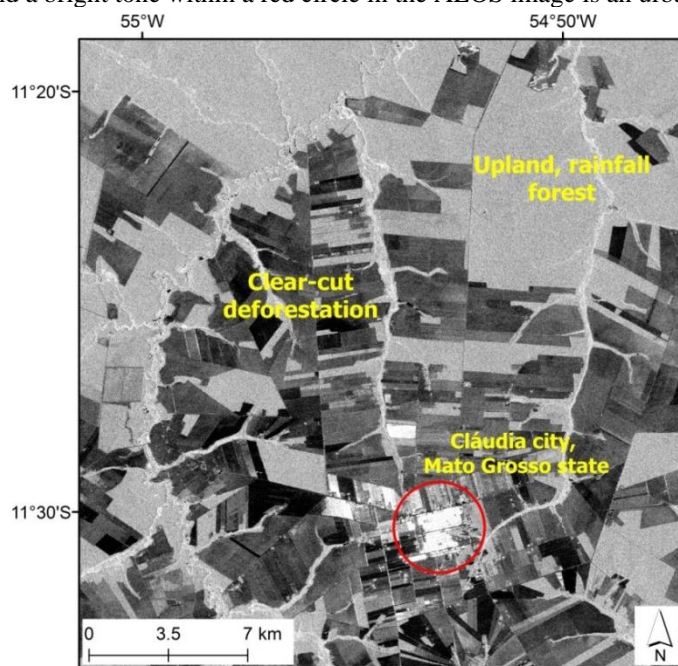
bright in radar images with HH polarization. This occurs because wood debris (trunks and branches) lying on the ground dry out and increase radar backscattering processes to higher values than those found in the surrounding primary forests (ALMEIDA-FILHO et al., 2005). Research conducted by Watanabe et al. (2018) showed that σ_{HH}° increased by 1.1–2.5 dB in areas with early-stage deforestation, while σ_{HV}° decreased by 0.7–1.0 dB. Therefore, any monitoring system with early warning for deforestation based on SAR dataset (e.g., the JICA-JAXA Forest Early Warning System in the Tropics - JJ-FAST) should not rely only on HV polarization. Another study by Reiche et al. (2015) indicated that the HV/HH ratio provided the most accurate results when deforested areas were compared with the Landsat normalized difference vegetation index (NDVI).

Figure 4 – Sentinel-1B SAR image obtained on September 4, 2019, VV polarization, showing suspicious features of oil spill from a platform of oil exploration in the Campos basin, north coast of Rio de Janeiro State.



Source: The authors (2020).

Figure 5 – ALOS-2 PALSAR-2 image from the Sinop region, Mato Grosso State, acquired on February 12, 2016, HH polarization, and 6.25 m of pixel spacing. Light gray is mostly composed by upland primary rainforests, dark gray is clear-cut deforestation, and a bright tone within a red circle in the ALOS image is an urban area (the city of Cláudia).



Source: The authors (2020).

Selective logging has been substantially increasing in tropical regions. Forest disturbances by logging

activities vary according to forest characteristics, logging intensity, and harvesting techniques (DYKSTRA, 2001; TRITSCH et al., 2016) and may severely impact forest ecosystems and increase forest susceptibility to fire (MONTEIRO et al., 2004; MATRICARDI et al., 2013; THOMPSON et al., 2013). Therefore, it is an important anthropogenic phenomenon to be monitored in tropical forests, commonly characterized by high cloud cover. SAR products can be useful to detect those forests impacted by logging activities in tropical regions. Jackson and Adam (2020) reported a total of 20 scientific articles using TerraSAR-X, ALOS-PALSAR, ENVISAT ASAR, TanDEM-X, Radarsat-2, COSMOSkyMed, and SAR airborne sensors to investigate selective logging worldwide. Most of these studies relied on SAR products and achieved high overall accuracies to map forests affected by selective logging. However, they have focused on particular study sites. A more comprehensive assessment of forest disturbances by selective logging is yet to be conducted and applied across the tropics. Subtle canopy changes and the capability to penetrate beyond the forest canopy seem to be the main constraint and technical challenge of using SAR products to detect forest impacts by logging activities.

6.3 Paddy rice monitoring

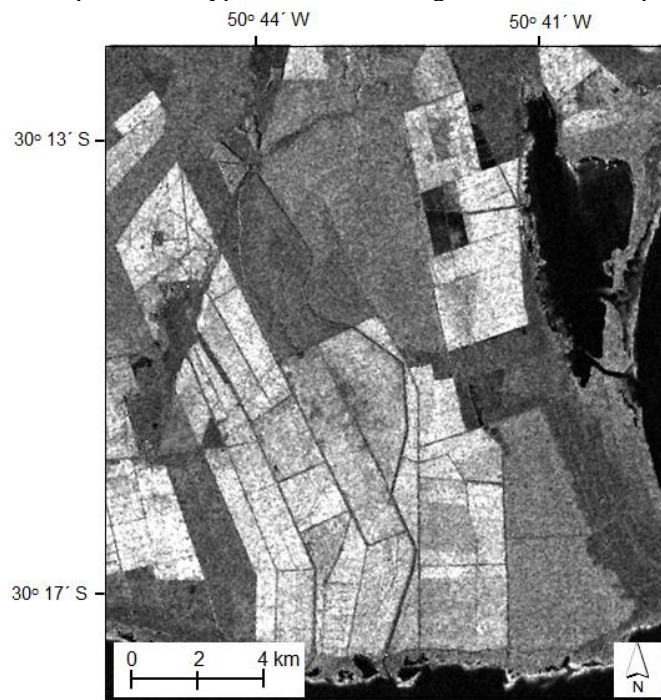
Rice is an important staple food in different countries of Asia (Bangladesh, China, Indonesia, Japan, Vietnam, and others). Rice paddies (semiaquatic cropping fields) cover more than 3 million hectares in China (WU et al., 2020). Paddy fields have also cultural value, as many were recognized as Globally Important Agricultural Heritage (LU; LI, 2006). In Brazil, rice paddy production is mainly found in the states of Rio Grande do Sul and Santa Catarina (STEINMETZ; BRAGA, 2001). The drawback is global warming, since paddy fields are a major source of methane, the second most influential greenhouse gas for climate change, after CO₂. SAR data have been intensely used for rice paddy detection, mapping, and yield estimation (e.g., KUROSU; FUJITA; CHIBA, 1995; LE TOAN et al., 1997; SINGHA et al., 2019). C-band, HV-polarization data has correlated significantly with the growing cycle of rice plantations (WU et al., 2011; YANG et al., 2012). At least three images are necessary during the rice growing season to properly estimate yields (WU et al., 2020). In this case, SAR data have good potential because of their independence of cloud conditions, as the rice cycle often overlaps the rainy season. Other authors (ISHITSUKA, 2018) stated that two images are required, one detecting water areas, and another with no detection of water. Fields exhibiting this temporal pattern can be associated with paddies planted with rice. During the peak of the growing cycle, rice fields appear bright in SAR images because of double bounce effects due to the presence of rice stems and waterlogging (Figure 6). Thus, such characteristics can be added in the approach developed by Ishitsuka (2018) to increase the accuracy of rice field identification.

6.4 Soil moisture estimation

Soil moisture estimation is one of the top-priority subjects in hydrology, since it is the key parameter controlling the interaction between atmosphere and land surface. However, its estimation using SAR technology has been somehow disappointing. Several studies were conducted in 1990's using empirical, semi-empirical, and physical-based theoretical models to retrieve soil moisture involving from semi-arid to moist temperate conditions, mostly using single sets of SAR data (e.g., ALTESE; BOLOGNANI; MANCINI, 1996; ULABY; DUBOIS; VAN ZYL, 1996; SANO et al., 1998b). The most recognized theoretical models are the integral equation model (IEM) and the small perturbation model (SPM), but they are rarely applied because of their low performance without prior knowledge of other parameters, such as soil roughness, for example (OUCHI, 2013). Empirical and semi-empirical models are often site-specific, relying on radar parameters and requiring a large amount of in situ datasets. In fact, taking into consideration the effects of soil roughness and vegetation cover is not an easy task. Due to the lack of operational, full-polarization capability of SARs to minimize the effects of soil roughness and vegetation, the results have not been satisfactory. In addition, accurate ground-truth data for validation are difficult to obtain because of the high spatial and temporal variability of this parameter. Nevertheless, recent initiatives have been focusing on this subject, such as the one led by Nicolas Baghdadi and collaborators from the University of Montpellier, France (BAGHDADI;

HOLAH; ZRIBI, 2006; BAGHDADI et al., 2016; EL HAJJ; BAGHDADI; ZRIBI, 2019). Basically, they are focusing on multi-frequency and multi-incidence angle data to obtain improved soil moisture estimations.

Figure 6 – Scene from the RADARSAT-1 satellite acquired on February 4, 1999 with 10-meter spatial resolution over the Lagoa dos Patos region, Rio Grande do Sul State, showing rice paddies (bright tones) due to double-bounce effects resulting of the simultaneous presence of rice stems and water layer. Darker shades of gray, adjacent to the rice fields, mostly correspond to the typical herbaceous vegetation of the Pampa biome.



Source: Mucenic (2001).

6.5 InSAR

The initial applications of InSAR were mainly focused on monitoring land displacements caused by earthquakes. One of the first practical demonstrations was conducted by Massonet et al. (1993), who used a pair of European Remote Sensing (ERS-1) SAR data (before and after the Landers, California earthquake occurred in June 28, 1992) to capture surface deformation along a 85-km fault system. The launch of Sentinel-1A and Sentinel-1B satellites facilitated the production of interferograms, allowing earthquake monitoring without observations provided by seismology. Funning and Garcia (2019) estimated, from literature search, the existence of more than 130 individual earthquakes monitored using InSAR data. Nevertheless, land deformation detection with InSAR is not always ensured, especially if decorrelation occurs. Decorrelation corresponds to reduction of interferometric correlation, a measure of coherence of the interferometric phase which can occur, for example, within certain surface conditions (e.g., dense vegetation or steep topography) (FUNNING; GARCIA, 2019).

More recently, the range of applications using this technique was extended mainly to detect landslides and land subsidence, with unprecedented resolution. These types of land deformation are related to the use of groundwater for human consumption, extraction of materials (e.g., mining activities and extraction of sands for civil construction), and human occupation of steep terrains, among others. Nowadays, the combination of data from several existing SAR satellites allows near daily monitoring of ground deformation caused by earthquakes or by humans. As pointed out by Biggs and Wright (2020), InSAR is transforming our understanding of faults, volcanoes, and ground stability, increasingly contributing to improve the feasibility of the hazard management activities.

7 CONCLUDING REMARKS

The relatively high number of SAR satellites launched during the last years and the ones planned to be launched are good indicators that the scientific community is convinced about the potential of radar remote sensing in several science fields. We believe that the great potential of radar imagery is not only because of its nearly all-weather imaging capability, but also because SAR imagery has been able to provide relevant information to users worldwide. At least two applications are strongly dependent on radar technology, oil spill monitoring using C-band and deforestation in tropical countries during wet season using L-band. The availability of TanDEM technology will allow deriving DEMs with improved accuracy and better resolution compared to the DEMs originally produced by the SRTM mission in 2000. The bistatic orbital SAR tomography is a very promising radar product to monitor deforestation in the tropics and other applications. However, more freely available/accessible SAR data acquired by sensors other than the Sentinel-1 are desired to encourage broader and heavier use of SAR data for different applications and research. As radar image processing is not an easy task, ready-to-use SAR products such as the radar vegetation index (RVI), a well-established microwave measurement for vegetation cover estimation, would be also helpful.

The use of constellation of SAR satellites seems to be an irreversible trend in the near future, as it can reduce revisit intervals, which have been a big issue in optical remote sensing. Nevertheless, radar users are still eager to have polarimetric capability installed in operational acquisition modes. The quad-pol capability is important because it allows more complex image processing, such as the decomposition of images into three or four components of different scattering mechanisms that cannot be achieved by amplitude data only. Interferometric SAR (InSAR) and differential SAR interferometry (DInSAR), which rely on phase information available in complex SAR images, will allow the monitoring of surface movements and deformation caused by earthquakes and volcanic activities with the accuracy of few millimeters. However, amplitude is the most basic type of SAR data; it seems that its use will continue for a while in various applications, including forest biomass estimation, deforestation monitoring, crop yield prediction, oil spill and ship detection, iceberg movement, and maritime traffic, among others.

One potential near-future application of SAR technology is the ship movement monitoring using the upcoming ALOS-4 satellite, scheduled to be launched in 2021. This satellite will be equipped with the Automatic Identification System (AIS) for ships. Thus, by combining these data with ALOS-4 SAR images, it will be possible to identify vessels whose tracking systems are turned off during the satellite overpass. Another potential application is the very high-resolution SAR sensors onboard the Unmanned Aerial Vehicles (UAVs) operating at Spotlight mode (5–10 cm) and at short microwave wavelengths (e.g., Ku-band) for target reconnaissance or even change detection studies.

Some of the challenging questions that future research in radar remote sensing must answer are:

- a) How dark patches in SAR images related to oil films and biogenic slicks present in ocean surfaces can be separated without on-site inspections or ancillary data?
- b) When the next generation SAR systems combining high spatial resolution (typically, 1 meter resolution) and timely datasets (typically, one week repeat pass) will be available, for example, for improved soil moisture, flooding, and crop yield monitoring?
- c) One of the best ways to make SAR data popular and readily available for global observation of dynamic processes on the Earth's surface is a web platform similar to the Google Earth™. When this dream will come true?

Authors' Contribution

E. E. Sano contributed in the conceptualization, data curation, writing, and reviewing processes. E. A. T. Matricardi and F. F. Camargo contributed in the writing and reviewing processes.

Conflicts of Interest

Authors declare that there is no conflict of interest.

References

- ALMEIDA-FILHO, R.; ROSENQVIST, A.; SHIMABUKURO, Y. E.; SANTOS, J. R. Evaluation and perspectives of using multitemporal L-band SAR data to monitor deforestation in the Brazilian Amazonia. **IEEE Geoscience and Remote Sensing Letters**, v. 2, n. 4, p. 409–412, 2005. DOI. 10.1109/LGRS.2005.856679
- ALPERS, W.; HOLT, B.; ZENG, K. Oil spill detection by imaging radars: Challenges and pitfalls. **Remote Sensing of Environment**, v. 201, p. 133–147, 2017. DOI. 10.1016/j.rse.2017.09.002
- ALSDORF, D. E.; SMITH, L. C.; MELACK, J. M. Amazon floodplain water level changes measured with interferometric SIR-C radar. **IEEE Transactions on Geoscience and Remote Sensing**, v. 39, n. 2, p. 423–431, 2001.
- ALTESE, E.; BOLOGNANI, O.; MANCINI, M. Retrieving soil moisture over bare soil from ERS 1 synthetic aperture radar data: Sensitivity analysis based on a theoretical surface scattering model and field data. **Water Resources Research**, v. 32, p. 653–661, 1996. DOI. 10.1029/95WR03638
- ALVES, S. A. S.; ASSANTE, L. R.; SANO, E. E.; MENESES, P. R. Abordagem metodológica baseada em imagens do SAR-R99B para identificar prováveis pistas de pouso não-homologadas na Amazônia. **Acta Amazonica**, v. 39, p. 723–726, 2009.
- ARGENTI, F.; LAPINI, A.; ALAPARONE, L. A tutorial on speckle reduction in synthetic aperture radar images. **IEEE Geoscience and Remote Sensing Magazine**, v. 1, n. 3, p. 6–35, 2013. DOI. 10.1109/MGRS.2013.2277512
- BAGHDADI, N.; HOLAH, N.; ZRIBI, M. Soil moisture estimation using multi-incidence and multi-polarization ASAR data. **International Journal of Remote Sensing**, v. 27, p. 1907–1920, 2006. DOI. <https://doi.org/10.1080/01431160500239032>
- BAGHDADI, N.; CHOKER, M.; ZRIBI, M.; EL HAJJ, M.; PALOSCIA, S.; VERHOEST, N. E. C.; LIEVENS, H.; BAUP, F.; MATTIA, F. A new empirical model for radar scattering from bare soil surfaces. **Remote Sensing**, v. 8, 920, 2016. DOI. 10.3390/rs8110920
- BAN, Y.; ZHANG, P.; NASCETTI, A.; BEVINGTON, A. R.; WULDER, M. A. Near real-time wildfire progression monitoring with Sentinel-1 SAR time series and deep learning. **Scientific Reports**, v. 10, 1322, 2020. DOI. 10.1038/s41598-56967-x
- BIGGS, J.; WRIGHT, T. J. How satellite InSAR has grown from opportunistic science to routine monitoring over the last decade. **Nature Communications**, v. 11, 3863, 2020. DOI. 10.1038/s41467-020-17587-6
- CAMARGO, F. F.; SANO, E. E.; ALMEIDA, C. M.; MURA, J. C.; ALMEIDA, T. A comparative assessment of machine-learning techniques for land use and land cover classification of the Brazilian tropical savanna using ALOS-2/PALSAR-2 polarimetric images. **Remote Sensing**, v. 11, 1600, 2019. DOI. 10.3390/rs11131600
- CARRINO, T. A.; SILVA, A. M.; BOTELHO, N. F.; SILVA, A. A. C. Lógica fuzzy e técnica SAM para modelagem previsional do ouro no setor oeste da Província Mineral de Tapajós usando dados aerogeofísicos e de sensoriamento remoto. **Revista Brasileira de Geofísica**, v. 29, p. 535–554, 2011.
- CANADA CENTRE FOR REMOTE SENSING (CCRS). **Fundamentals of Remote Sensing**. Available at: <https://www.nrcan.gc.ca/sites/www.nrcan.gc.ca/files/earthsciences/pdf/resource/tutor/fundam/pdf/fundamentals_e.pdf>. Accessed: 16 Oct. 2020.
- CIMINO, J.; ELACHI, C.; SETTLE, M. SIR-B – The second shuttle imaging radar experiment. **IEEE Transactions on Geoscience and Remote Sensing**, v. 24, n. 4, p. 445–452, 1986. DOI. 10.1109/TGRS.1986.289658
- CLOUDE, S. R.; POTTIER, E. An entropy based classification scheme for land applications of polarimetric SAR. **IEEE Transactions on Geoscience Remote Sensing**, v. 35, n. 1, p. 68–78, 1997. DOI. 10.1109/36.551935

- COVELLO, F.; BATTAZZA, F.; COLETTA, A.; LOPINTO, E.; FIORENTINO, C.; PIETRANERA, L.; VALENTINI, G.; ZOFFOLI, S. COSMO-SkyMed an existing opportunity for observing the Earth. **Journal of Geodynamics**, v. 49, n. 3-4, p. 171–180, 2010. DOI. 10.1016/j.jog.2010.01.001
- CANADIAN SPACE AGENCY (CSA). **Technical features of the RCM**. Available at: <<https://www.asc-csa.gc.ca/eng/satellites/radarsat/technical-features/default.asp>>. Accessed: 29 Jul. 2020.
- DECHESENE, C.; LEFÈVRE, S.; VALDAINE, R.; HAJDUCH, G.; FABLET, R. Ship identification and characterization in Sentinel-1 SAR images with multi-task deep learning. **Remote Sensing**, v. 11, n. 24, 2997, 2019. DOI. 10.3390/rs11242997
- DOBSON, M. C.; PIERCE, L. E.; ULABY, F. T. Knowledge-based land-cover classification using ERS-1/JERS-1 SAR composites. **IEEE Transactions on Geoscience and Remote Sensing**, v. 34, n. 1, p. 83–99, 1996. DOI. 10.1109/36.481896
- DYKSTRA, D. P. Reduced impact logging: concepts and issues. *In*: INTERNATIONAL CONFERENCE, 2001, Kuching, Malaysia. **Proceedings...** Bangkok: FAO, 2001. 526 p.
- EL HAJJ, M.; BAGHDADI, N.; ZRIBI, M. Comparative analysis of the accuracy of surface soil moisture estimation from the C- and L-bands. **International Journal of Applied Earth Observation and Geoinformation**, v. 82, 101888, 2019. DOI. 10.1016/j.jag.2019.05.021
- ENVI. **Sentinel-1 Intensity Analysis in ENVI SARscape Tutorial**. Available at: <<https://www.harrisgeospatial.com/portals/0/pdfs/Sentinel1IntensityAnalysisTutorial.pdf>>. Accessed: 29 Jul. 2020.
- EUROPEAN SPACE AGENCY (ESA). **Sentinel Application Platform (SNAP). SNAP 6.0 Help Guide**. ESA, 2018.
- EUROPEAN SPACE AGENCY (ESA). **Sentinel-1 Toolbox. SAR Basics Tutorial**. Paris: ESA, 2019, 19 p.
- EUROPEAN SPACE AGENCY (ESA). **SAOCOM**. Available at: <<https://directory.eoportal.org/web/eoportal/satellite-missions/s/saocom>>. Accessed: 29 Jul. 2020.
- EVANS, D. L. Spaceborne imaging radar –C/X-band synthetic aperture radar (SIRC/X-SAR): a look back on the tenth anniversary. **IEE Proceedings – Radar, Sonar and Navigation**, v. 153, n. 2, p. 81–86, 2006. DOI. 10.1049/ip-rsn:20045095
- EVANS, D. L.; ALPERS, W.; CAZENAVE, A.; ELACHI, C.; FARR, T.; GLACKIN, D.; HOLT, B.; JONES, L.; LIU, W. T.; McCANDLESS, W.; MENARD, Y.; MOORE, R.; NJOKU, E. Seasat – A 25-year legacy of success. **Remote Sensing of Environment**, v. 94, p. 384–404, 2005. DOI. 10.1016/j.rse.2004.09.011
- FERRAZZOLI, P.; PALOSCIA, S.; PAMPALONI, P.; SCHIAVON, G.; SIGISMONDI, S.; SOLIMINI, D. The potential of multifrequency polarimetric SAR in assessing agricultural and arboreous biomass. **IEEE Transactions on Geoscience and Remote Sensing**, v. 35, n. 1, p. 5–17, 1997. DOI. 10.1109/36.551929
- FOX, P. A.; LUSCOMBE, A. P.; THOMPSON, A. A. RADARSAT-2 SAR modes development and utilization. **Canadian Journal of Remote Sensing**, v. 30, n. 3, p. 258–264, 2004. DOI. 10.5589/m04-014
- FREEMAN, A.; DURDEN, S. L. A three-component scattering model for polarimetric SAR Data. **IEEE Transactions on Geoscience and Remote Sensing**, v. 36, n. 3, p. 963–973, 1998. DOI. 10.1109/36.673687
- FUNNING, G. J.; GARCIA, A. A systematic study of earthquake detectability using Sentinel-1 Interferometric Wide-Swath data. **Geophysical Journal International**, v. 216, p. 332–349, 2019. DOI. 10.1093/gji/ggy426
- GUERRA, J. B.; MURA, J. C.; FREITAS, C. C. Discriminação de incrementos de desflorestamento na Amazônia com dados SAR R99B em banda L. **Acta Amazonica**, v. 40, p. 557–566, 2010.
- HAGENSIEKER, R.; WASKE, B. Evaluation of multi-frequency SAR images for tropical land cover mapping. **Remote Sensing**, v. 10, 257, 2018. DOI. 10.3390/rs10020257
- HANSEN, R. F. **Radar Interferometry: Data Interpretation and Error Analysis**. New York: Kluwer Academic Publishers, 2002, 308 p.
- HELLMANN, M. P. **SAR polarimetry tutorial**. Rennes: University of Rennes, 2001. 109 p. Available at:

<<http://epsilon.nought.de/>>. Accessed: 02 Aug. 2020.

- HENDERSON, F. M.; LEWIS, A. J. **Principles & Applications of Imaging Radar. Manual of Remote Sensing**. Nova York: John Wiley & Sons, 3rd ed., v. 2, 1998.
- HESS, L. L.; MELACK, J. M.; FILOSO, S.; WANG, Y. Delineation of inundated area and vegetation along the Amazon floodplain with SIR-C synthetic aperture radar. **IEEE Transactions on Geoscience and Remote Sensing**, v. 33, n. 4, p. 896–903, 1995. DOI. 10.1109/36.406675
- HUBER, S.; ALMEIDA, F. Q.; VILLANO, M.; YOUNIS, M.; KRIEGER, G.; MOREIRA, A. Tandem-L: A technical perspective on future spaceborne SAR sensors for Earth observation. **IEEE Transactions on Geoscience and Remote Sensing**, v. 56, n. 8, p. 4792–4807, 2018. DOI. 10.1109/TGRS.2018.2837673
- INSTITUTO BRASILEIRO DE GEOGRAFIA E ESTATÍSTICA (IBGE). Biblioteca. Catálogo. Rio de Janeiro: IBGE. Available at: <<https://biblioteca.ibge.gov.br/index.php/biblioteca-catalogo?acervo=todos&campo=todos¬qry=&opeqry=&texto=RADAMBRASIL&digital=false&fra seexata=>>>. Accessed: 29 Jul. 2020.
- ISHITSUKA, N. Identification of paddy rice areas using SAR: Some case studies in Japan. **Japan Agricultural Research Quarterly**, v. 52, n. 3, p. 197–204, 2018. DOI. 10.6090/jarq.52.197
- IVANOV, Y. Y. Assessment of marine oil pollution using Kosmos-1980 and Almaz-1 radar images. **Mapping Sciences and Remote Sensing**, v. 35, n. 3, p. 202–217, 1998. DOI. 10.1080/07493878.1998.10642092
- JACKSON, C. M.; ADAM, E. Remote sensing of selective logging in tropical forests: Current state and future directions. **iForest – Biogeosciences and Forestry**, v. 13, p. 286–300, 2020. DOI. 10.3832/ifer3301-013
- JAXA. Japan Aerospace Exploration Agency. **ALOS-2 basic observation scenario (second edition rev.A)**. Tsukuba: JAXA, 2017, 35 p.
- JENSEN, J. R. **Remote Sensing of the Environment. An Earth Resources Perspective**. Upper Saddle River: Prentice Hall Inc., 2000.
- KASISCHKE, E. S.; MELACK, J. M.; DOBSON, M. C. The use of imaging radars for ecological applications - a review. **Remote Sensing of Environment**, v. 59, n. 2, p. 141–156, 1997. DOI. 10.1016/S0034-4257(96)00148-4
- KOYAMA, C. N.; WATANABE, M.; HAYASHI, M.; OGAWA, T.; SHIMADA, M. Mapping the spatial-temporal variability of tropical forests by ALOS-2 L-band SAR big data analysis. **Remote Sensing of Environment**, v. 233, 111372, 2019. DOI. 10.1016/j.rse.2019.111372
- KRIEGER, G.; MOREIRA, A.; FIEDLER, H.; HAJNSEK, I.; WERNER, M.; YOUNIS, M.; ZINK, M. TanDEM-X: A satellite formation for high-resolution SAR interferometry. **IEEE Transactions on Geoscience and Remote Sensing**, v. 45, n. 11, p. 3317–3341, 2007. DOI. 10.1109/TGRS.2007.900693
- KRIEGER, G.; ZINK, M.; BACHMANN, M.; BRÄUTIGAM, B.; SCHULZE, D.; MARTONE, M.; RIZZOLI, P.; STEINBRECHER, U.; ANTONY, J. W.; DE ZAN, F.; HAJNSEK, I.; PAPATHANASSIOU, K.; KUGLER, F.; CASSOLA, M. R.; YOUNIS, M.; BAUMGARTNER, S.; LÓPEZ-DEKKER, P.; PRATS, P.; MOREIRA, A. TanDEM-X: A radar interferometer with two formation-flying satellites. **Acta Astronautica**, v. 89, p. 83–98, 2013. DOI. 10.1016/j.actaastro.2013.03.008
- KUROSU, T.; FUJITA, M.; CHIBA, K. Monitoring of rice crop growth from space using the ERS-1 C-band SAR. **IEEE Transactions on Geoscience and Remote Sensing**, v. 33, n. 4, p. 1092–1096, 1995. DOI. 10.1109/36.406698
- LA ROSA, L. E. C.; FEITOSA, R. Q.; HAPP, P. N.; SANCHES, I. D.; COSTA, G. A. O. P. Combining deep learning and prior knowledge for crop mapping in tropical regions from multitemporal SAR image sequences. **Remote Sensing**, v. 11, 2029, 2019. DOI. 10.3390/rs11172029
- LAVROVA, O. Y.; KOSTIANOV, A. G. Catastrophic oil spill in the Gulf of Mexico in April-May 2010. **Izvestiya, Atmospheric and Oceanic Physics**, v. 47, n. 9, p. 1114–1118, 2011. DOI. 10.1134/S0001433811090088

- LE TOAN, T.; RIBBES, F.; WANG, L. F.; FLOURY, N.; DING, K. H.; KONG, J. A.; FUJITA, M. Rice crop mapping and monitoring using ERS-1 data based on experiment and modeling results. **IEEE Transactions on Geoscience and Remote Sensing**, v. 35, n. 1, p. 41–56, 1997. DOI. 10.1109/36.551933
- LEE, J.; POTTIER, E. **Polarimetric Radar Imaging: from Basics to Applications**. New York: CRC Press, 2009, 398 p.
- LEIFER, I.; LEHR, W. J.; SIMECEK-BEATTY, D.; BRADLEY, E.; CLARK, R.; DENNISON, P.; HU, Y.; MATHESON, S.; JONES, C. E.; HOLT, B.; REIF, M.; ROBERTS, D. A.; SVEJKOVSKY, J.; SWAYZE, G.; WOZENCRAFT, J. State of the art satellite and airborne marine oil spill remote sensing: Application to the BP *Deepwater Horizon* oil spill. **Remote Sensing of Environment**, v. 124, p. 185–209, 2012. DOI. 10.1016/j.rse.2012.03.024
- LI, H.; HE, Y.; WANG, W. Improving ship detection with polarimetric SAR based on convolution between co-polarization channels. **Sensors**, v. 9, n. 2, p. 1221–1236, 2009. DOI. 10.3390/s90201221
- LIMA, M. I. C. **Projeto Radam: Uma Saga Amazônica**. Belém: Paka-Tatu, 2014.
- LU, J.; LI, X. Review of rice-fish-farming systems in China – One of the Globally Important Ingenious Agricultural Heritage Systems (GIAHS). **Aquaculture**, v. 260, n. 1–4, p. 106–113, 2006. DOI. 10.1016/j.aquaculture.2006.05.059
- MANDAL, D.; KUMAR, V.; RATHA, D.; DEY, S.; BHATTACHARYA, A.; LOPEZ-SANCHEZ, J. M.; McNAIRN, H.; RAO, Y. S. Dual polarimetric radar vegetation index for crop growth monitoring using Sentinel-1 SAR data. **Remote Sensing of Environment**, v. 247, 111954, 2020. DOI. 10.1016/j.rse.2020.111954
- MARTONE, M.; RIZZOLI, P.; WECKLICH, C.; GONZÁLEZ, C.; BUESO-BELLO, J. L.; VALDO, P.; SCHULZE, D.; ZINK, M.; KRIEGER, G.; MOREIRA, A. The global forest/non-forest map from TanDEM-X interferometric SAR data. **Remote Sensing of Environment**, v. 205, p. 352–373, 2018. DOI. 10.1016/j.rse.2017.12.002
- MASSONNET, D.; ROSSI, M.; CARMONA, C.; ADRAGNA, F.; PELTZER, G.; FEIGL, K.; RABAUTE, T. The displacement field of the Landers earthquake mapped by radar interferometry. **Nature**, v. 364, 6433, p. 138–142. DOI. 10.1038/364138a0
- MATRICARDI, E. A. T.; SKOLE, D. L.; PEDLOWSKI, M. A.; CHOMENTOWSKI, W. Assessment of forest disturbances by selective logging and forest fires in the Brazilian Amazon using Landsat data. **International Journal of Remote Sensing**, v. 34, p. 1057–1086, 2013. DOI: 10.1080/01431161.2012.717182
- MIGLIACCIO, M.; NUNZIATA, F.; MONTUORI, A.; PAES, R. L. Single-look complex COSMO-SkyMed SAR data to observe metallic targets at sea. **IEEE Journal of Selected Topics in Applied Earth Observations and Remote Sensing**, v. 5, n. 3, p. 893–901, 2012. DOI. 10.1109/JSTARS.2012.2184271
- MONTEIRO, A. L. S.; SOUZA Jr., C. M.; BARRETO, P. G.; PANTOJA, F. L. S.; GERWING, J. J. Impactos da exploração madeireira e do fogo em florestas de transição da Amazônia Legal. **Scientia Forestalis**, n. 65, p. 11–21, 2004.
- MOREIRA, A.; KRIEGER, G.; HAJNSEK, I.; PAPATHANASSIOU, K.; YOUNIS, M.; LOPEZ-DEKKER, P.; HUBER, S.; VILLANO, M.; PARDINI, M.; EINEDER, M.; DE ZAN, F.; PARIZZI, A. Tandem-L: A highly innovative bistatic SAR mission for global observation of dynamics processes on the Earth's surface. **IEEE Geoscience and Remote Sensing Magazine**, v. 3, n. 2, p. 8–23, 2015. DOI. 10.1109/mgrs.2015.2437353
- MUCENIC, N. **Uso do radar (banda C) no mapeamento de arroz irrigado no estado do Rio Grande do Sul** (Mestrado em Sensoriamento Remoto), Porto Alegre: Universidade Federal do Rio Grande do Sul, 2001.
- MURA, J. C.; PARADELLA, W. R.; DUTRA, L. V.; SANTOS, J. R.; RUDORFF, B. F. T.; MIRANDA, F. P.; SILVA, M. M. Q.; SILVA, W. F. MAPSAR image simulation based on L-band polarimetric data from the SAR-R99B airborne sensor (SIVAM system). **Sensors**, v. 9, p. 102–117, 2009. DOI.

10.3390/s90100102

- NANNINI, M.; MARTONE, M.; RIZZOLI, P.; PRATS-IRAOLA, P.; RODRIGUEZ-CASSOLA, M.; REIGBER, A.; MOREIRA, A. Coherence-based SAR tomography for spaceborne applications. **Remote Sensing of Environment**, v. 225, p. 107–114, 2019. DOI. 10.1016/j.rse.2019.01.040
- NURTYANWAN, R.; FERDIYANTI, G. A.; BUDIHARTO, A.; WIKANTIKA, K. Modelling of surface roughness on agriculture area using Radarsat-2 satellite. **IOP Conference Series: Earth and Environmental Science**, v. 500, 012080, 2020. DOI. 10.1088/1755-1315/500/1/012080
- OUCHI, K. Recent trend and advance of synthetic aperture radar with selected topics. **Remote Sensing**, v. 5, p. 716–807, 2013. DOI. 10.3390/rs5020716
- PARADELLA, W. R.; SANTOS, A. R.; VENEZIANI, P.; CUNHA, E. S. P. Radares imageadores nas geociências: Estado da arte e perspectivas. **Revista Brasileira de Cartografia**, v. 57, n. 1, p. 56–62, 2005.
- PEREIRA, L. O.; FREITAS, C. C.; SANT'ANNA, S. J. S.; REIS, M. S. ALOS/PALSAR data evaluation for land use and land cover mapping in the Amazon region. **IEEE Journal of Selected Topics in Applied Earth Observations and Remote Sensing**, v. 9, n. 12, p. 5413–5423, 2016. DOI. 10.1109/JSTARS.2016.2622481
- PINTO, W. H. A.; LUCHIARI, A. Uso das imagens SAR R99B para mapeamento geomorfológico do canal do Ariaú no município de Iraduba-AM. **Revista de Geografia**, v. 34, p. 209–229, 2017.
- PITZ, W.; MILLER, D. The TerraSAR-X satellite. **IEEE Transactions on Geoscience and Remote Sensing**, v. 48, n. 2, p. 615–622, 2010. DOI. 10.1109/TGRS.2009.2037432
- PULELLA, A.; SANTOS, R. A.; SICA, F.; POSOVSKY, P.; RIZZOLI, P. Multi-temporal Sentinel-1 backscatter and coherence for rainfall mapping. **Remote Sensing**, 12, 847, 2020. DOI. 10.3390/rs12050847
- REICH, J.; VERBESSELT, J.; HOEKMAN, D.; HEROLD, M. Fusing Landsat and SAR time series to detect deforestation in the tropics. **Remote Sensing of Environment**, v. 156, p. 276–293, 2015. DOI. 10.1016/j.rse.2014.10.001
- RICHARDS, J. A. **Remote Sensing with Imaging Radar**. Berlin: Springer, 2009. 361 p.
- RIZZOLI, P.; MARTONE, M.; GONZALEZ, C.; WECKLICH, C.; TRIDON, D. B.; BRAUTIGAM, B.; BACHMANN, M.; SCHULZE, D.; FRITZ, T.; HUBER, M.; WESSEL, B.; KRIEGER, G.; ZINK, M.; MOREIRA, A. Generation and performance assessment of the global TanDEM-X digital elevation model. **ISPRS Journal of Photogrammetry and Remote Sensing**, v. 132, p. 119–139, 2017. DOI. 10.1016/j.isprsjprs.2017.08.008
- ROSENQVIST, A.; SHIMADA, M.; LUCAS, R.; CHAPMAN, B.; PAILLOU, P.; HESS, L.; LOWRY, J. The Kyoto & Carbon Initiative – a brief summary. **IEEE Journal of Selected Topics in Applied Earth Observations and Remote Sensing**, v. 3, n. 4, p. 551–553, 2010. DOI. 10.1109/JSTARS.2010.2086270
- ROSENQVIST, A.; SHIMADA, M.; SUZUKI, S.; OHGUSHI, F.; TADONO, T.; WATANABE, M.; TSUZUKU, K.; WATANABE, T.; KAMIJO, S.; AOKI, E. Operational performance of the ALOS global systematic acquisition strategy and observation plans for ALOS-2 PALSAR-2. **Remote Sensing of Environment**, v. 155, p. 3–12, 2014. DOI. 10.1016/j.rse.2014.04.011
- SAATCHI, S. S.; SOARES, J. V.; ALVES, D. S. Mapping deforestation and land use in Amazon rainforest by using SIR-C imagery. **Remote Sensing of Environment**, v. 59, p. 191–202, 1997. DOI. 10.1016/S0034-4257(96)00153-8
- SANO, E. E.; FERREIRA, L. G.; HUETE, A. R. Synthetic aperture radar (L-band) and optical vegetation indices for discriminating the Brazilian savanna physiognomies: a comparative analysis. **Earth Interactions**, v. 9, 15, 2005. DOI. 10.1175/EI117.1
- SANO, E. E.; MENESES, P. R.; ALMEIDA, T. Reflectância dos alvos na faixa de micro-ondas. In: MENESES, P. R.; ALMEIDA, T.; BAPTISTA, G. M. M. (Orgs.). **Reflectância dos Materiais Terrestres. Análise e Interpretação**. São Paulo: Oficina de Textos, Cap. 10, 2019. p. 291–315.

- SANO, E. E.; HUETE, A. R.; TROUFLEAU, D.; MORAN, M. S.; VIDAL, A. Relation between ERS-1 synthetic aperture radar data and measurements of surface roughness and moisture content of rocky soils in a semiarid rangeland. **Water Resources Research**, v. 34, n. 6, p. 1491–1498, 1998a. DOI. 10.1029/98WR00032
- SANO, E. E.; MORAN, M. S.; HUETE, A. R.; MIURA, T. C- and multiangle Ku-band synthetic aperture radar data for bare soil moisture estimation in agricultural areas. **Remote Sensing of Environment**, v. 64, p. 77–90, 1998b. DOI. 10.1016/S0034-4257(97)00170-3
- SARMAP. **SARSCAPE**. Caslano: SARMAP, 2020. Available at: <http://www.sarmap.ch/wp/index.php/software/sarscape/>. Accessed: 3 Aug. 2020.
- SCHLUND, M.; ERASMI, S. Sentinel-1 time series data for monitoring the phenology of winter wheat. **Remote Sensing of Environment**, v. 246, 111814, 2020. DOI. 10.1016/j.rse.2020.111814
- SILVA, A. Q.; PARADELLA, W. R.; FREITAS, C. C.; OLIVEIRA, C. G. Evaluation of digital classification of polarimetric SAR data for iron-mineralized laterites mapping in the Amazon region. **Remote Sensing**, v. 5, p. 3101–3122, 2013. DOI. 10.3390/rs5063101
- SILVA, V. S.; SANO, E. E.; ALMEIDA, T.; MESQUITA JÚNIOR, H. N. Discriminação de classes de cobertura vegetal em uma região de transição Amazônia/Cerrado no estado de Mato Grosso por meio de imagens do satélite ALOS-2/PALSAR-2. **Revista Brasileira de Cartografia**, 2020, in press.
- SINGHA, M.; DONG, J.; ZHANG, G.; XIAO, X. High resolution paddy rice maps in cloud-prone Bangladesh and Northeast India using Sentinel-1 data. **Scientific Data**, v. 6, 2019. DOI: 10.1038/s41597-019-0036-3
- SOUZA-FILHO, P. W. M.; PARADELLA, W. R.; RODRIGUES, S. W. P.; COSTA, F. R.; MURA, J. C.; GONÇALVES, F. D. Discrimination of coastal wetland environments in the Amazon region based on multi-polarized L-band airborne synthetic aperture radar imagery. **Estuarine, Coastal and Shelf Science**, v. 95, p. 88–98, 2011. DOI. 10.1016/j.ecss.2011.08.011
- SRIVASTAVA, H. S.; PATEL, P.; MANCHANDA, M. L.; ADIGA, S. Use of multi-incidence angle RADARSAT-1 SAR data to incorporate the effect of surface roughness in soil moisture estimation. **IEEE Transactions on Geoscience and Remote Sensing**, v. 41, n. 7, p. 1638–1640, 2003. DOI. 10.1109/TGRS.2003.813356
- STEINMETZ, S.; BRAGA, H. J. Zoneamento de arroz irrigado por épocas de semeadura nos estados do Rio Grande do Sul e de Santa Catarina. **Revista Brasileira de Agrometeorologia**, v. 9, n. 3, p. 429–438, 2001.
- STONE, T. A.; WOODWELL, G. M. Shuttle imaging radar. An analysis of land use in Amazonia. **International Journal of Remote Sensing**, v. 9, n. 1, p. 95–105, 1988. DOI. 10.1080/01431168808954839
- TAKAKU, J.; TADONO, T.; TSUTSUI, K. Generation of high resolution global DSM from ALOS PRISM. **The International Archives of the Photogrammetry, Remote Sensing and Spatial Information Sciences**, v. XL-4, p. 243–248, 2014. DOI. 10.5194/isprsarchives-XL-4-243-2014
- THOMPSON, I. D.; GUARIGUATA, M. R.; OKABE, K.; BAHAMONDEZ, C.; NASI, R.; HEYMELL, V.; SABOGAL, C. An operational framework for defining and monitoring forest degradation. **Ecology and Society**, v. 18, n. 2, 20, 2013. DOI. 10.5751/ES-05443-180220
- TORRES, R.; SNOEIJ, P.; GEUDTNER, D.; BIBBY, D.; DAVIDSON, M.; ATTEMA, E.; POTIN, P.; ROMMEN, B.; FLOURY, N.; BROWN, M.; TRAVER, I. N.; DEGHAJE, P.; DUESMANN, B.; ROSICH, B.; MIRANDA, N.; BRUNO, C.; L'ABBATE, M.; CROCI, R.; PIETROPAOLO, A.; HUCHLER, M.; ROSTAN, F. GMES Sentinel-1 mission. **Remote Sensing of Environment**, v. 120, p. 9–24, 2012. DOI. 10.1016/j.rse.2011.05.028
- TRITSCH, I.; SIST, P.; NARVAES, I. S.; FREITAS, L. J. M.; BLANC, L.; BOURGOIN, C.; CORNU, G.; GOND, V. Multiple patterns of forest disturbance and logging shape forest landscape in Paragominas, Brasil. **Forests**, v. 7, 315, 2016. DOI: 10.3390/f7120315
- ULABY, F. T.; BATLIVALA, P. P. Optimum radar parameters for mapping soil moisture. **IEEE**

- Transactions on Geoscience Electronics**, v. 14, n. 2, p. 81–93, 1976. DOI. 10.1109/TGE.1976.294414
- ULABY, F. T.; DUBOIS, P. C.; VAN ZYL, J. Radar mapping of surface soil moisture. **Journal of Hydrology**, v. 184, p. 57–84, 1996. DOI. 10.1016/0022-1694(95)02968-0
- VALENZUELA, G. R. Theories for the interaction of electromagnetic and oceanic waves – a review. **Boundary-Layer Meteorology**, v. 13, n. 1–4, p. 61–85, 1978. DOI. 10.1007/BF00913863
- VAN DER SANDEN, J. J. **Radar remote sensing to support tropical forest management** (Ph.D. thesis in Agronomy), 1997, Wageningen: Wageningen Agricultural University, 1997, 330 p.
- WATANABE, M.; KOYAMA, C. N.; HAYASHI, M.; NAGATANI, I.; SHIMADA, M. Early-stage deforestation detection in the tropics with L-band SAR. **IEEE Journal of Selected Topics in Applied Earth Observations and Remote Sensing**, v. 11, n. 6, p. 2127–2133, 2018. DOI. 10.1109/JSTARS.2018.2810857
- WU, F.; WANG, C.; ZHANG, H.; ZHANG, B.; TANG, Y. Rice crop monitoring in South China with RADARSAT-2 quad-polarization SAR data. **IEEE Geoscience and Remote Sensing Letters**, v. 8, n. 2, 2011. DOI. 10.1109/LGRS.2010.2055830
- WU, X.; LIU, L.; GUO, X.; LIU, Z.; LI, K.; SHAO, Y. Comparison of water cloud models with different layers for rice yield estimation from a single TerraSAR image. **Remote Sensing Letters**, v. 11, n. 9, p. 876–882, 2020. DOI. 10.1080/2150704X.2020.1781284
- YAMAGUCHI, Y.; MORIYAMA, T.; ISHIDO, M.; YAMADA, H. Four-component scattering model for polarimetric SAR image decomposition. **IEEE Transactions on Geoscience Remote Sensing**, v. 43, n. 8, p. 1699–1706, 2005. DOI. 10.1109/TGRS.2005.852084
- YANG, S.; ZHAO, X.; LI, B.; HUA, G. Interpreting RADARSAT-2 quad-polarization SAR signatures from rice paddy based on experiments. **IEEE Geoscience and Remote Sensing Letters**, v. 9, n. 1, p. 65–69, 2012. DOI. 10.1109/LGRS.2011.2160613
- ZHANG, M.; CHEN, F.; LIANG, D.; TIAN, B.; YANG, A. Use of Sentinel-1 GRD SAR images to delineate flood extent in Pakistan. **Sustainability**, v. 12, 5784, 2020. DOI. 10.3390/su12145784
- ZINK, M.; BACHMANN, M.; BRÄUTIGAM, B.; FRITZ, T.; HAJNSEK, I.; KRIEGER, G.; MOREIRA, A.; WESSEL, B. TanDEM-X: The new global DEM takes shape. **IEEE Geoscience and Remote Sensing Magazine**, v. 2, n. 2, p. 8–23, 2014. DOI. 10.1109/mgrs.2014.2318895

Authors' biography



Edson Eyji Sano, Echaporã/SP – Brazil, 1958. Geologist graduated from the University of São Paulo (USP), São Paulo/SP, M.Sc. in Remote Sensing from the National Institute for Space Research (INPE), São José dos Campos/SP, and Ph.D. in Soil Science from the University of Arizona, Tucson/Arizona. Researcher at Embrapa Cerrados since 1989. His research interest is in the area of agricultural and environmental monitoring using optical and radar remote sensing, mainly in the Cerrado and Amazon biomes.



Eraldo Aparecido Trondoli Matricardi, Presidente Prudente/SP, Brazil, 1963. Forest Engineer graduated from the Federal University of Mato Grosso (UFMT), Cuiabá/MT, specialist in Remote Sensing from the Federal University of Santa Maria (UFSM), Santa Maria/RS, M.Sc. and Ph.D. in Geography from Michigan State University (MSU), USA. Associate Professor at the University of Brasília (UnB), since 2009. His research interest is in the area of forest degradation and land use and land cover changes using remote sensing data, climate change, and landscape analysis.



Flávio Fortes Camargo, Curitiba/PR – Brazil, 1978. Geographer graduated from the University of São Paulo (USP), São Paulo/SP, M.Sc. in Remote Sensing from the National Institute for Space Research (INPE), São José dos Campos/SP, and Ph.D. in Applied Geosciences and Geodynamics from the University of Brasília (IG-UnB), Brasília/DF. Analyst in Transport Infrastructure at DNIT since 2013. His research interest is in the area of geomorphology and land use and land cover changes using optical and radar remote sensing and artificial intelligence.



Esta obra está licenciada com uma Licença [Creative Commons Atribuição 4.0 Internacional](https://creativecommons.org/licenses/by/4.0/) – CC BY. Esta licença permite que outros distribuam, remixem, adaptem e criem a partir do seu trabalho, mesmo para fins comerciais, desde que lhe atribuam o devido crédito pela criação original.